ORIGINAL ARTICLE

Microseismic events on the Åknes rockslide in Norway located by a back-projection approach

Tomáš Fischer · **Daniela Kühn** · **Michael Roth**

Abstract The Åknes rockslide in Western Norway is characterised by a steady movement of a rock mass with an extent of about 1 km^2 and a yearly deformation rate in the range of 2 to 4 cm. A seismic network consisting of 8 three-component geophones records tens to hundreds of local and distant seismic events daily. Depending on their character, local seismic events show a variety of waveforms, both with abrupt and emergent onsets. Along with the relatively low frequencies of the waveforms, standard location procedure using arrival time measurements is difficult to apply. Based on the event envelopes, we classify local events and obtain their approximate location by stacking STA/LTA ratios of back-projected waveforms. To suppress the influence of complex surface morphology and related complicated wave propagation, we constrain hypocentres to the surface of the slope and determine only horizontal coordinates. The method was successfully tested by locating two types of ground truth data: calibration shots and a block collapse. The test proved the ability of the method to determine the position of sliding events with an uncertainty of less than 36 m, which allows to distinguish amongst several foci of rockslide activity. Application of the method to 8 years of monitoring data shows continuous seismic activity, which is concentrated in the centre and at the western edge of the monitored area. Most likely, microseismic events recorded by the seismic network originate within the body of the rock slope and are related to its disintegration or potentially to sliding on the detachment fault.

Keywords Stacking · Back-projection · Microseismicity · Rockslide · Hazard · Åknes · STA/LTA

T. Fischer
Faculty of Science, Charles University, Prague, Czech Republic

T. Fischer
Institute of Geophysics, Czech Academy of Sciences, Prague, Czech Republic

D. Kühn
NORSAR, Kjeller, Norway

D. Kühn (✉)
GFZ German Research Centre for Geosciences, Potsdam, Germany
e-mail: daniela@norsar.no

M. Roth
Swedish National Seismic Network, Department of Earth Sciences, Geophysics, Villav. 16, 752 36 Uppsala, Sweden

1 Introduction

Seismic monitoring of rockslides using an on-site seismic network is recently becoming a common tool for improving our understanding of the processes driving slope movement in order to enhance the level of civil protection. Spillmann et al. (2007) used a network of 12 geophones to monitor the activity of an unstable mountain slope in the Swiss Alps and determined locations of about 220 microearthquakes using a non-linear location approach applied on P-wave arrival time picks. A strong correlation between rainfall and activity of the Séchilienne rockslide in the French Alps was found by

Helmstetter and Garambois ([2010]). Lacroix and Helmstetter ([2011]) applied a beamforming technique to the records of three small seismic arrays at the Séchilienne rockslide to locate the events; in total, 55 microearthquakes and an even higher number of rock-falls were located with errors below 50 m. The Slum-gullion landslide in Colorado was investigated by a short experiment including amongst others a dense 88-station network (Gomberg et al. [2011]). It was shown that the landslide basal surface beneath the seismic network slipped almost aseismically and that seismic signals originated from the side-bounding strike-slip faults. Collapses of cavities are also accompanied by series of seismic events, whose locations help to image the process of detachment of the cavity roof (e.g. Kinscher et al. [2014]). Integration of ground deformation and microseismic monitoring helped to assess slope unstability in an open-pit mine in Queensland, Australia (Salvoni and Dight [2016]). The subject of the current study is seismic monitoring of the Åknes unstable rock slope in Norway (Fig. [1]), which is one of the most investigated and best monitored rockslides in the world.

1.1 The Åknes site

The rockslide is located on the western flank of Sunnylvsfjord, a branch of Storfjorden, in the Møre and Romsdal County of Western Norway. Since large portions of the sliding volume can be released as a whole, hurtling of the rock mass into the fjord may cause a large tsunami threatening several nearby settlements. Rock avalanches and related tsunamis represent a serious natural hazard in Norway (Blikra et al. [2006]). During the twentieth century, three major tsunami disasters occurred due to sub-aerial rockslides within the fjord region in the western part of Norway (Loen, 1905 and 1936; Tafjord, 1934) with maximum run-up heights between 40 and 74 m. Historical records from the last 400 years show that in average, two to three catastrophic events take place per century, claiming 250 lives in total (Blikra et al. [2006]). Within the same period, 12 large rockslides befell the inner Storfjorden area (Blikra et al. [2006]) and a swath bathymetry revealed a minimum of 59 slope failures since the last glaciation (10,000 years ago; Blikra et al. [2005]).

Tsunami analyses of the Åknes rockslide including laboratory experiments and numerical simulations indicate a maximum run-up height of 70 m for Geiranger and 85 m for Hellesylt for the maximum credible worst-case scenario of a rockslide of 54 million m^3 volume. For a second scenario, assuming the rockslide only comprises the western flank, the maximum run-up height still amounts to 30 m for Geiranger and 35 m for Hellesylt for 18 million m^3 of volume (Harbitz et al. [2014]).

Due to increased coastal population, development and tourism, future events will most likely be even more disastrous than indicated by historical records (Harbitz et al. [2014]). For example, 150 to 200 cruise ships and more than 700,000 tourists visit the nearby Geirangerfjord, registered on UNESCO's world heritage list, every year (www.visitnorway.com). The town of Stranda, just 15 km northwest of the rockslide area, has 3500 inhabitants. The rockslide tsunami hazard and the tsunami early warning system related to the unstable slopes at Åknes and Hegguraksla (close to the 1934 Tafjord rockslide site) are managed by the Åknes/Tafjord Beredskap IKS (previously the Åknes/Tafjord project). A more detailed overview on tsunami hazard in the northeast Atlantic including Norwegian fjords as well as on other projects worldwide with relevance for rockslide tsunami risk assessment and management is given in Harbitz et al. ([2014]).

1.2 Previous studies

A variety of measurement techniques has been applied to the slope, amongst other geophysical methods (2D resistivity, ground penetrating radar, refraction seismics, geophysical logging of boreholes) as well as hydrological and geological methods (drilling, mapping, multi-tracer tests); for details, see e.g. Ganerød et al. ([2008]), Oppikofer et al. ([2009]) and Heincke et al. ([2010]).

Continuous monitoring is performed by rod extensometers, differential GPS, instrumented boreholes, two single lasers for distance measurements across the uppermost tension cracks, periodic laser scanning (ground-based LiDAR), ground-based INSAR (in summertime), satellite-based radar, a microseismic network of geophones, an automated total station with 30 prisms, a weather station and web cameras (ÅTB [2010]).

The slope consists mainly of quartzo-feldspatic gneisses (Braathen et al. [2004]). Three distinct fracture sets were identified by Ganerød et al. ([2008]): two sets of fractures running normal to the foliation (trending N-S and E-W, respectively) as well as fractures occurring parallel to the foliation. This last set of fractures runs in
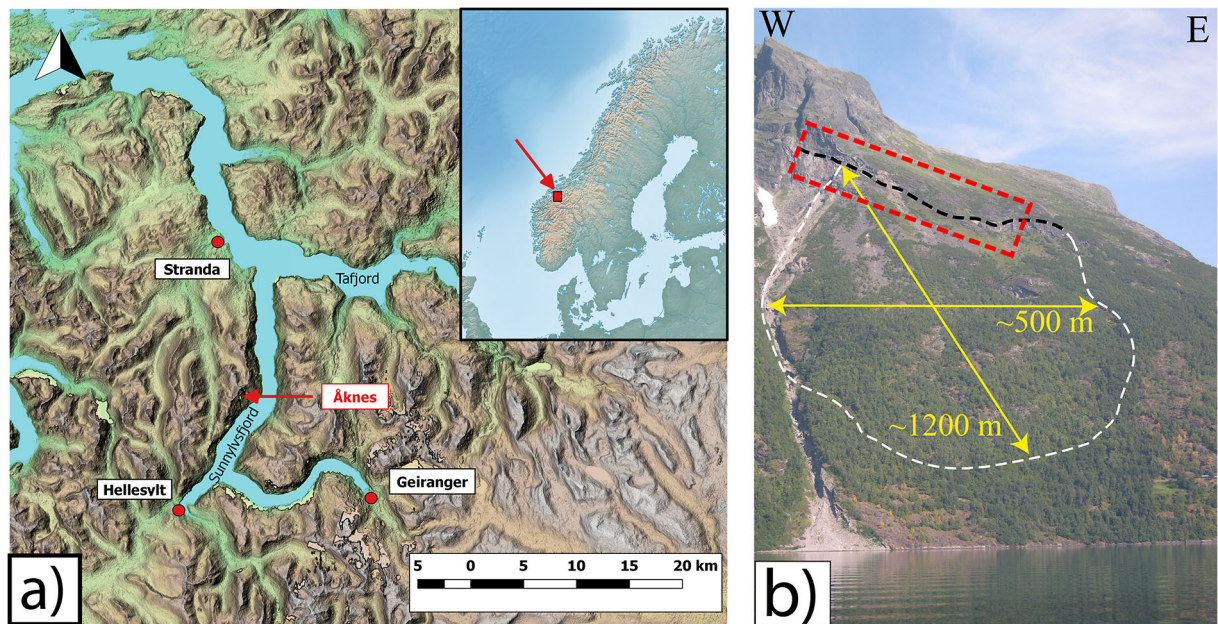
Fig. 1 **a** Location of the Åknes rockslide in Western Norway. (Map: MapSurfer ASTER GDEM-SRTM hillshade combined with 10 m resolution DTM downloaded from https://www.geonorge.no/. Inset: cross-blended hypso downloaded from http://www.naturalearthdata.com/.) **b** Slope with the unstable area indicated by a white dashed line and the back scarp marked by a black dashed line; the placement of the seismic network is indicated by the red dashed rectangle. Adapted from Heincke et al. (2010), photograph: Mark Derron

addition sub-parallel to the steeply dipping slope (up to 35°) and thus constitutes the main reason for the slope instability (Ganerød et al. 2008). Slide scars in the mountainside indicate previous slide activity (Kveldsvik et al. 2008).

The unstable area reaches from 100 to 900 m a.s.l. (Fig. 1), confined by a large-scaled back scarp extending in E-W direction (Ganerød et al. 2008), and is estimated to be 500 m wide across slope and 1200 m down-slope (Heincke et al. 2010). The back scarp (or 'upper tension crack') is 800 m long. It progresses eastwards, where it has an opening of 0.5 to 1 m and widens to an opening of 2 to 3 m further to the west (Grøneng et al. 2011). The volume of the entire unstable rock mass is still uncertain, but has been estimated to 54 million m^3 by Blikra et al. (2013), to 60–80 million m^3 by Kveldsvik (2008) and to 20–85 million m^3 by Nordvik et al. (2009). The uncertainty mainly results from the fact that the depth of the basal sliding plane is still under discussion: Blikra et al. (2013) assume a depth of 50 m, Kveldsvik (2008) suggests a depth of 120 m and Nordvik et al. (2009) discuss three scenarios with depths of an undulating sliding plane at 40–55 m, 105–115 m and 150–190 m.

Displacement rates are highest close to the back scarp and decrease towards the toe zone and the eastern part of the rockslide: they amount to 14 cm/a beneath the back scarp (Heincke et al. 2010) and decrease to 2–4 cm/a in the upper central part (Ganerød et al. 2008). In the lower part, a positive elevation change of 1–3 cm/a is measured associated with compressional movements (Ganerød et al. 2008).

Movements on the slope are strongly influenced by water infiltration; thus, the hydrogeological regime is considered as a critical factor affecting the slope stability (Heincke et al. 2010). Very high flow rates (17.4 m/h) measured during a multi-tracer test show that the unstable rock slope is highly permeable due to intense fracturing (Frei 2008). Grøneng et al. (2011) analysed meteorological parameters for their influence on rock deformation from 2004 throughout August 2008. Air temperature and precipitation turned out to govern phases of increasing and decreasing displacement. Snow melting periods cause the largest annual deformation event and in autumn, periods with heavy precipitation in combination with air temperature fluctuations around 0 °C seem to cause acceleration phases. However, during the 2nd half of the observation period, other processes seem to have become more important than the meteorological effects (disintegration of irregularities along unfilled joints and disintegration of intact rock bridges

in the sliding plane; Grøneng et al. 2011). The extensometers exhibit a high correlation of displacement with groundwater level as well (Nordvik et al. 2009).

2 Data

In October 2005, a seismic network has been installed consisting of eight 3-C geophones (Geospace Technologies, type GS-11D; 4.5 Hz eigenfrequency) covering an area of about 250 × 150 m in the upper part of the unstable slope (Figs. 1 and 2). The stations are connected with the central acquisition system installed in a concrete bunker by armoured cables. The acquisition system customised by NORSAR engineers includes a 24-channel digitizer (Geode, Geometrics), a GPS clock, an industry computer with

low-power consumption and a GSM telephone relay. It is powered by a set of batteries, which in turn is charged by a diesel generator. The system is connected to a radio link that bridges the 13 km distance to the village of Hellesylt, and from there, a secure VPN connection to NORSAR has been established. Recording parameters of the acquisition system can be modified remotely at any time. Data from the eight 3-C geophones are recorded with a sampling rate of 1000 Hz (125 Hz until 5 August 2006) and are transferred in near real time (1–2 min delay) to NORSAR, where automatic event detection is performed. An event is defined if the signal-to-noise ratio is larger than 2 on at least 10 channels within a common time window of 1 s length. The resulting triggered data are stored, and their characteristics are computed and are forwarded to the early warning centre (http://www.aknes.no/) (with 5–10 min
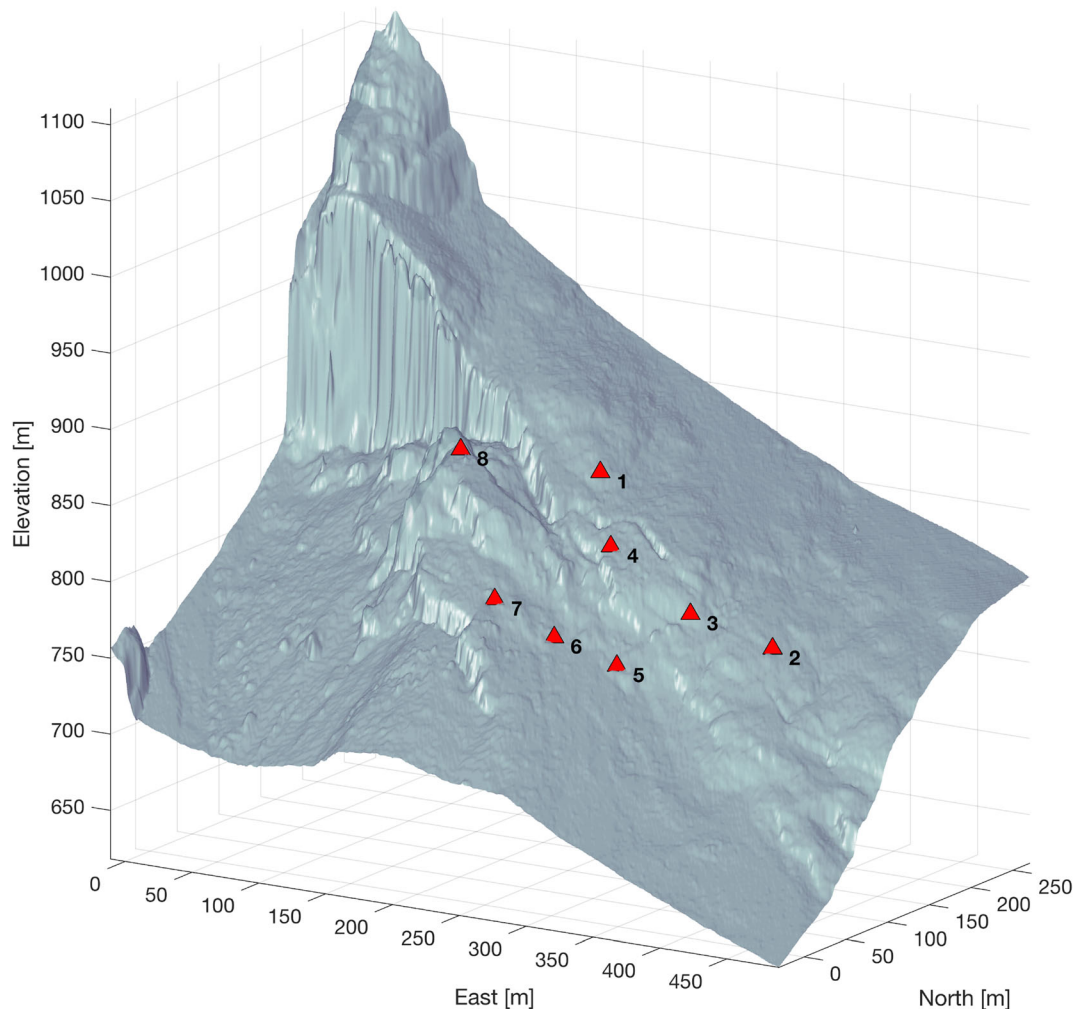

Fig. 2 Digital elevation model showing the placement of the eight 3-C geophones composing the seismic network

delay). The system became operational in November 2005 and is performing very stable. For the whole period of interest of 8 years, at least 18 of the in total 24 channels were available at all times (Fig. 3). Outages were mostly caused by lightning or damaged cables cut by rockfalls. Geophones 6 and 7 (channels 16–21) are most prone to outages, since their cabling crosses a swath experiencing frequent rockfalls. Since November 2009, the broadband station AKN (Guralp CMG-3ESPC, 60 s to 100 Hz) is operational in addition.

Apart from regional earthquakes and mining blasts, between 3100 and 6500 local seismic events are recorded annually. Until now, standard microseismic event location was not successful due to the complex velocity structure of the upper slope and high uncertainty of arrival time measurements on the seismograms. In August 2006, an active seismic calibration experiment using eleven shot positions was performed, which showed strong local variations of velocities that did not allow to develop a coherent velocity model. Trials to locate the events employing arrival times under assumption of a homogeneous velocity model were not successful.

In this paper, we apply an automatic procedure for identifying local seismic events and implement a back-projection stacking method for determining hypocentre locations. We find that for the back-projection stacking location, the homogeneous model calibrated using surface shots from August 2006 including the topography

of the slope is sufficient. We apply the method to 8 years of seismic monitoring data. The locations of microseismic events and rockfalls on the rock slope are analysed and compared with the ground truth information on a block collapse in the eastern part of the monitored area.

3 Methods

3.1 Event classification

Firstly, the events were classified in order to remove electronic spikes and distant events. The electronic spike identification was based on the fact that these are pulses of very short duration that occur on all traces simultaneously, dominate the seismograms and are present on the majority of traces. Thus, they were identified by stacking the normalised absolute value of traces: in case of a spike occurrence, the maximum amplitude approaches the number of traces.

Secondly, the events were classified into four types according to their origin: microseismic events, rockfalls and avalanches, distant events and noise. To this end, we used several criteria characterising the signal in the time and frequency domains. The classification in time domain was based on the signal envelope stacked across all traces; due to the small interstation distance, the phase onset delays are very small between stations
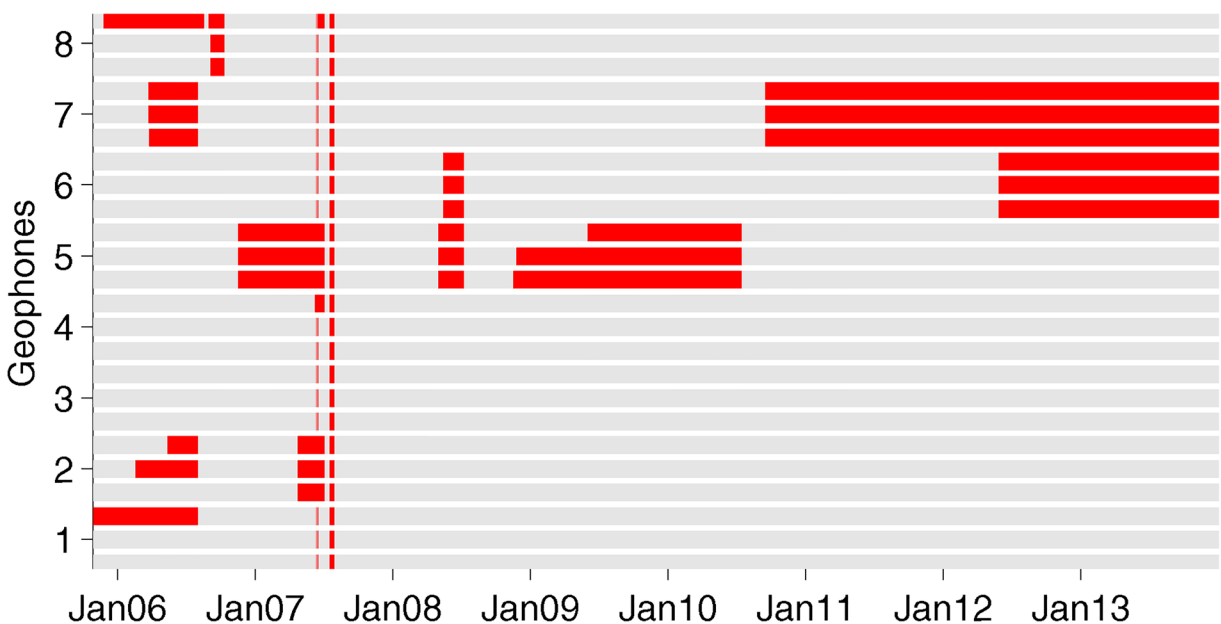

Fig. 3 Up- and downtimes (grey and red bars, respectively) of the Åknes network geophones. *x*-axis denotes years of recordings

(Fig. 4) and the traces may be stacked without the need for applying a time shift reflecting the slowness of the arriving waves. From the resulting global envelope, the following parameters were measured: (a) number of peaks, (b) width of the main peak, (c) maximum amplitude, (d) distribution of amplitudes amongst stations and (e) duration of elevated amplitude level. In frequency domain, the ratio of amplitude spectrum for frequencies higher and lower than 20 Hz was determined (f). The combination of parameters (a)–(f) was investigated employing a weighting scheme resulting in a probability of the event belonging to the four individual event classes. The characteristic distribution of parameters for the four event types was obtained by manual classification of about 1000 events and applied subsequently to the whole data set. The result of this procedure is a list of events of local origin (microseismic events and rockfalls) that are subject to hypocentre location.

Examples of a rockfall occurring between geophones no. 1 and 2 and of a local microseismic event close to geophone no. 4 (channels 10–12) are displayed in Fig. 4. The prevailing frequency of the local events ranges

between 20 and 50 Hz and may strongly vary amongst stations, depending on the epicentral distance.

3.2 Microseismic event location

The large complexity of recorded seismograms renders traditional processing in terms of arrival time picking and linearised inversion for location difficult. In particular, some events are recorded on few stations only, some waveforms are missing impulsive onsets (Fig. 5) and the frequency content of the waveforms strongly varies amongst stations (e.g. geophones no. 2 and 3 in Fig. 5), probably due to the strongly heterogeneous structure within the fracture zones that subdivide the seismic network into several segments. In addition, the small network aperture places high demands on the precision of arrival time measurements, which suffer from frequent emergent onsets of wave arrivals. For a typical local seismic network of an aperture of 20 km, P- and S-wave travel times are in the order of seconds and the errors in arrival time measurements range up to 0.01 s (i.e. much less than 1%). The travel times in the Åknes network, however, are lower than
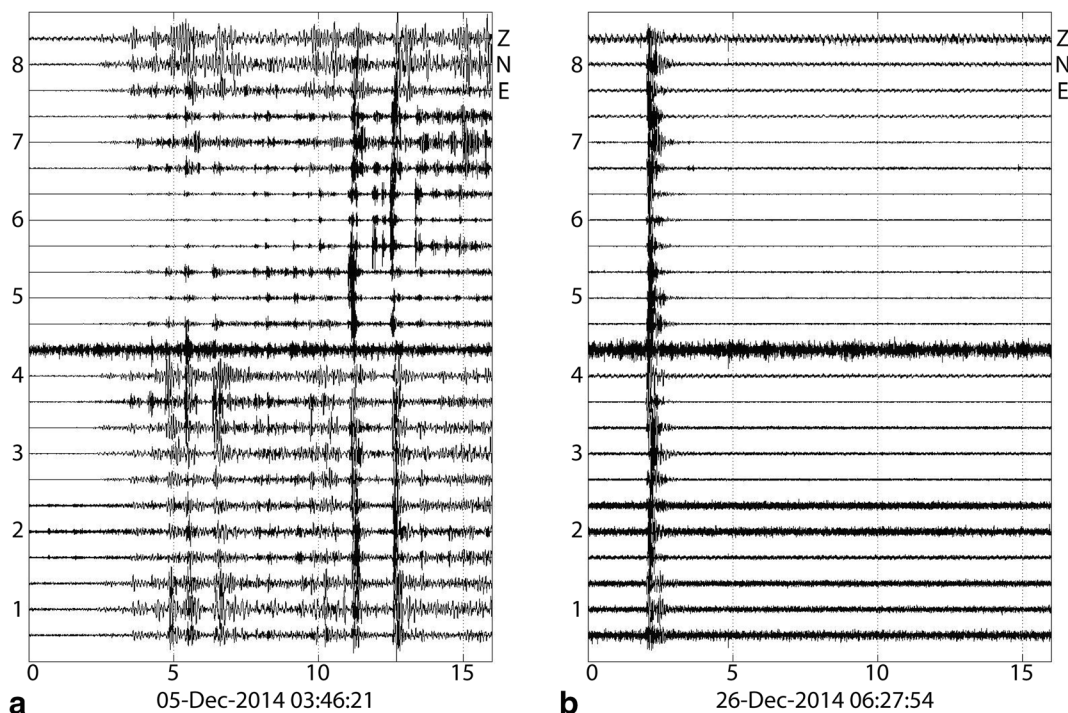

Fig. 4 Sample seismograms of a rockfall (**a**) and a microseismic event (**b**) recorded on the geophone network; for each of the 8 stations, the Z, N and E components are shown. The horizontal axis shows time in seconds

Fig. 5 Typical waveforms of a microseismic event; grey traces were out of order, and amplitudes are normalised for each channel. Note the emergent onset and a long-period waveform at geophone no. 3, which is the second closest to the epicentre close to geophone no. 2 showing the highest frequencies
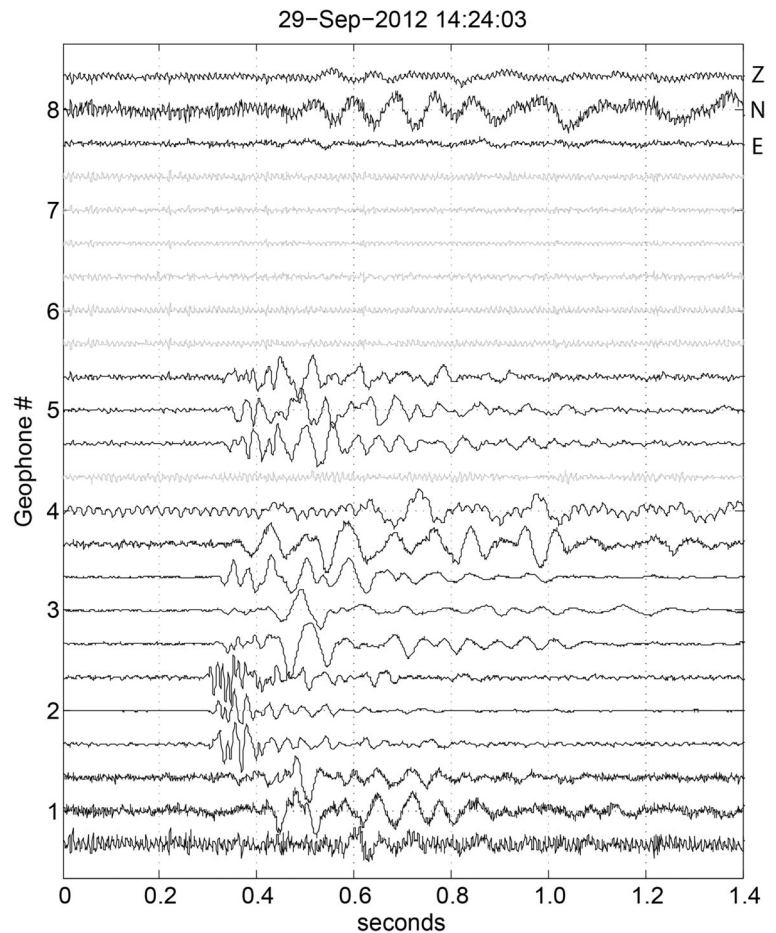
0.1 s for events occurring within the network (assuming a P-wave velocity of 1500 m/s) and the accuracy of arrival time measurement is not better than in the case of a typical local network implying that within the Åknes network, the arrival time errors amount to more than 10% of the travel times; more than 10 times larger than for a typical local seismic network. The situation is hampered further by missing S-waves, which makes the standard method of arrival time picking unsuitable for location of microseismic events recorded on the Åknes network.

In order to avoid standard arrival time measurements, we implemented a back-projection stacking (also termed migration stacking) method, which does not require arrival times and exploits instead the energy of arriving seismic waves. Back-projection stacking methods use various characteristic functions derived from the seismograms affecting the success of the event location. The first implementation of a back-projection method by Kao and Shan (2007) stacked the mean absolute

amplitude (so-called brightness) in a short time window at different stations. Gharti et al. (2010) computed the envelope of seismic traces rotated to the ray coordinates and performed a stacking along P and S arrival times. The use of short-term-average/long-term-average (STA/LTA) ratios for seismic event location has been introduced by Withers et al. (1999), who proposed a correlation-based method to locate seismic events at regional scale. Grigoli et al. (2014) used STA/LTA of the vertical component as a P-wave characteristic function. Stacking STA/LTA proved also suitable for back-projection location of induced events recorded at dense surface arrays (Vlček et al. 2016). Based on tests, we found the STA/LTA function most suitable for back-projection stacking of the Åknes data, because it highlights the phase arrival onsets. This appears useful especially in our case of relatively long seismograms, whose duration (~ 0.5 s) exceeds significantly the time difference between wave arrivals at neighbouring stations (< 0.03 s). We use non-

overlapping windows of 8 ms and 80 ms durations for the STA and LTA, respectively. Compared with other detector functions as, e.g. kurtosis or Akaike information criterion, which give sharp narrow maxima at the phase onset, the STA/LTA characteristic function appears more suitable for stacking. The reason is that it only slightly highlights the onset while keeping sufficient pulse width such that the pulses at different stations overlap even in the case of delays caused by unknown heterogeneities in the velocity model.

Back-projection stacking Our stacking approach is not very different from other back-projection or source-scanning algorithms. According to the expected location errors, we choose a grid with 20 m grid spacing in the space of unknown hypocentre coordinates $(x_0, y_0)_k$ and shift the seismograms of different geophones i to the origin time t_0^{ik} that corresponds to the investigated grid point k. The shifted traces are stacked using their STA/LTA ratios R_i to construct an objective function

$$S_k = \sum_i R_i\left(t - t_0^{ik}\right), \tag{1}$$

where t is the observed arrival time and t_0^{ik} is the theoretical origin time. Because of the complicated polarisation pattern of the seismograms, we treat all three components similarly—we sum over all traces independent of their orientation. Due to the less pronounced S-waves and in order to estimate the location of events for which only few traces of sufficient quality are available, we assume events to occur close to the surface, such that only two unknowns (x_0, y_0) are searched. For event depth, the slope topography is taken into account, such that z_0 is determined by the digital elevation model. The optimum location corresponds to the grid point with the maximum value of the stack S_{max}. Prior to stacking, the STA/LTA ratios R are not normalised so that stations with high R contribute more to the stack. The reason is that this suppresses the influence of noisy stations and helps to locate events with only few contributing stations. We further test the quality of the location by comparing the maximum

Fig. 6 Location procedure. **a** Unshifted STA/LTA traces (thin black lines) and stack S_0 with zero time shift (blue dashed line). **b** Optimally shifted STA/LTA traces (thin black lines) resulting in maximum stack S_{max} after back projection to the hypocentre (blue dashed line). Note the larger amplitude and smaller width of S_{max} compared with S_0; a stack enhancement η of 1.24 was achieved. **c** Map of objective function S_k; the weighted location (determined by Eq. (4)) is shown as a cross with size equal to the estimated location error; the stack maximum is indicated by a red circle. Triangles indicate geophones—geophones coloured white were used for location, the ones coloured black were out of order
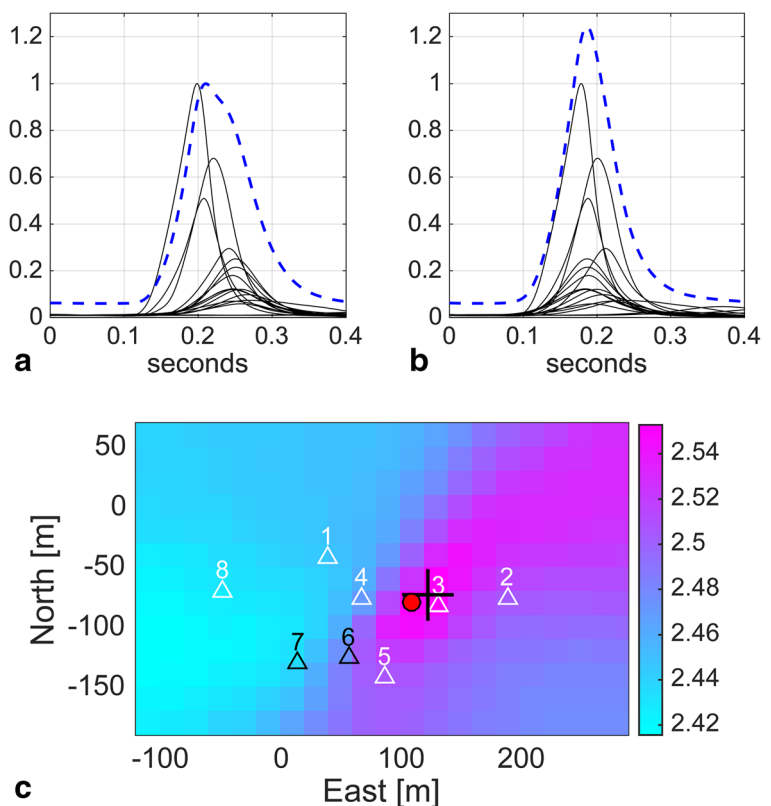
stack with the stack S_0 obtained without applying a time shift (Fig. 6)

$$S_0 = \sum_i R_i(t) \qquad (2)$$

and, similar to Vlček et al. (2016), define the stack enhancement ratio

$$\eta = S_{max}/S_0 \qquad (3)$$

indicating the success of event location within the network.

Stack enhancement The behaviour of stack enhancement is illustrated in Fig. 7. For vertical incidence of seismic wave with zero slowness, the onset times are identical at all geophones and therefore, any stack enhancement η is lower than 1 for all grid points. This holds true also in the case of electronic spikes (Fig.

7a), which arrive simultaneously at all geophones. For all other seismic sources, the stack enhancement η is larger than 1 (Fig. 7b, c). Values $\eta \approx 1$ are expected also for local disturbances occurring near individual geophones. Similar to the root-mean-square error of the fit of arrival times in the standard earthquake location techniques, the stack enhancement η represents a measure of location quality. In fact, η primarily increases with increasing fit of theoretical and measured arrival times. Thus, although we do not measure arrival times directly, they are contained in the occurrence time of the maximum of the characteristic function R_i at individual geophones.

Optimum location and error estimate The grid spacing of 20 m results in a grid of 13×21 grid points and thus, in a rather coarse pattern of epicentres. Besides, the objective functions show an asymmetric shape, especially if their maxima occur outside the seismic network. To take this
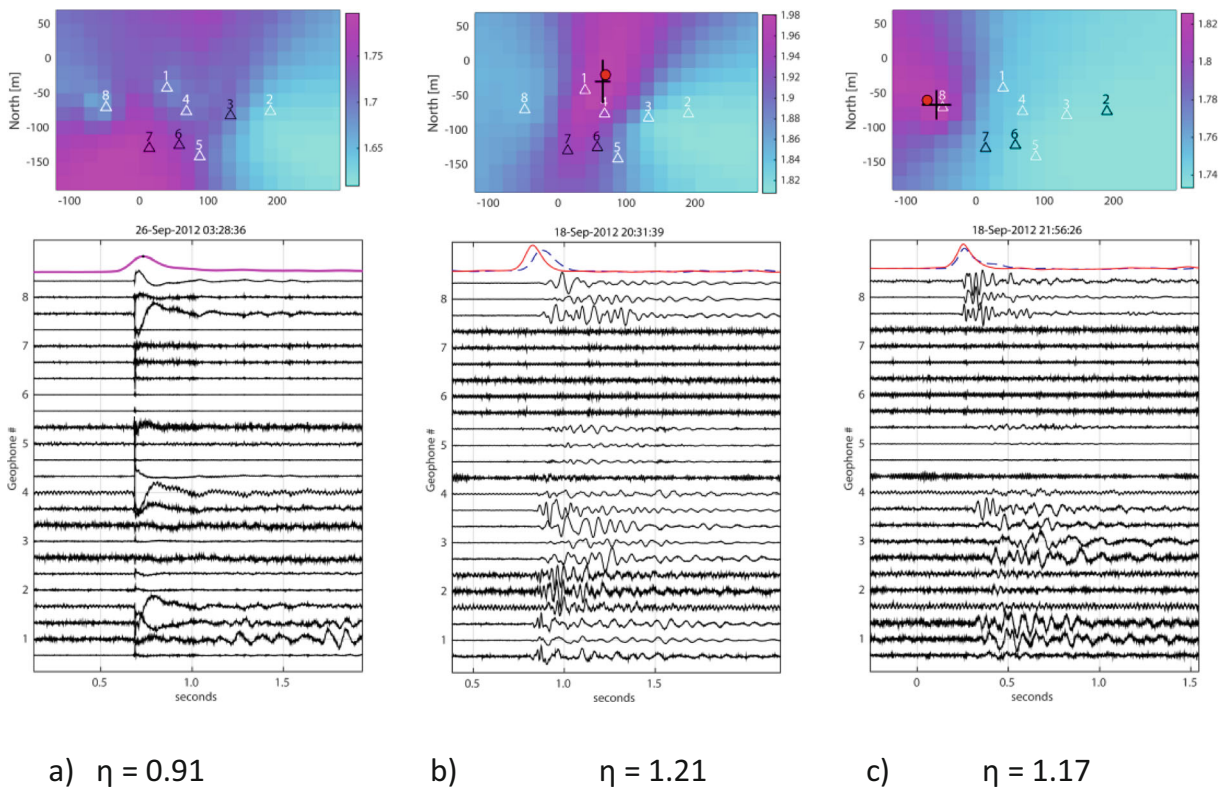

a) η = 0.91   b)   η = 1.21   c)   η = 1.17

Fig. 7 Maps of the STA/LTA stack S_k (top) and waveforms (bottom) of three typical seismic signals with characteristic stack enhancement η: **a** electric spike, $\eta < 1$; **b** and **c** microseismic events with different hypocentres, $\eta \geq 1$. On the waveform panel, the top curves show stacks S_0 with zero time shift (blue dashed line) and S_{max} after back projection to the hypocentre (red line). See caption of Fig. 6 for details

into account, we define the optimum location as the centroid of the objective function for the interval of coordinates for which the objective function exceeds a selected level of its maximum. Accordingly, the centroid coordinates are obtained as weighted averages

$$x_0 = \frac{\sum\limits_{ij} S(x_i, y_j) x_i}{\sum\limits_{ij} S(x_i, y_j)}, \tag{4}$$

and similarly for y_0, for i, j where

$$S(x_i, y_j) > 0.8 \max(S). \tag{5}$$

The location uncertainty is estimated as the spatial width of the objective function in terms of mean distance from the epicentre in the x and y directions to the positions where the objective function decreases below the level of 0.8 S_{max}. This way of estimating location errors reflects both the uncertainty in the velocity model (in terms of mismatch of the back-projected objective function maxima caused by mismatch of the observed and calculated travel times) as well as the uncertainty of
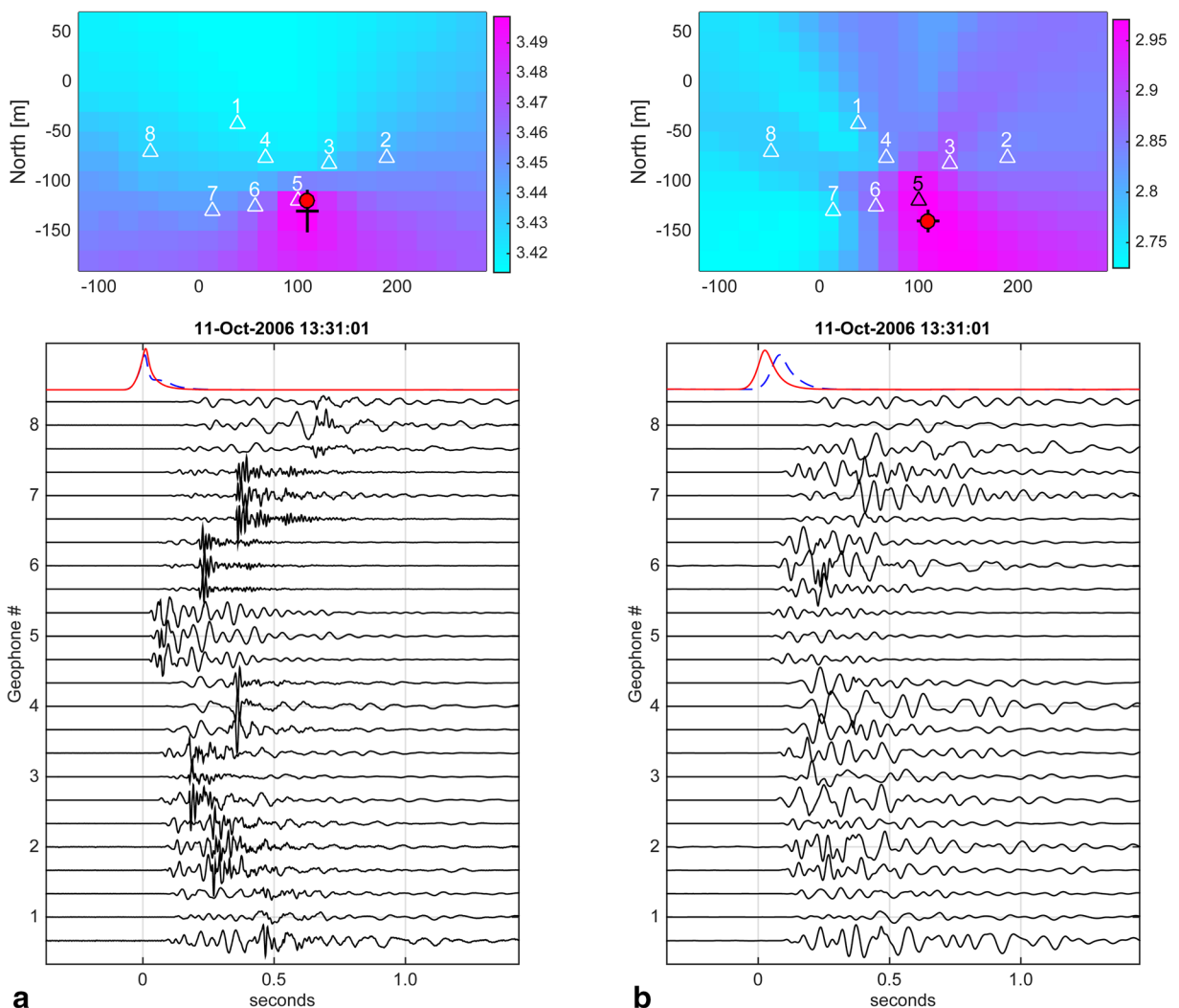

Fig. 8 Waveforms of a calibration shot close to geophone no. 5: **a** unfiltered and **b** low-pass filtered up to 40 Hz. Note in (**a**) the high-frequency acoustic phases with later arrival than the seismic phases. The location procedure is not affected by the sound wave because the STA/LTA detector highlights the onset of the faster seismic wave. See caption of Fig. 7 for details

measuring arrival times (in terms of the width of the maximum of the objective function in time domain at different stations). However, it should be noted that the choice of the level of 80% is arbitrary and thus, the location error estimates must be interpreted only relatively to each other, not as absolute location error.

3.3 Calibration of the location method using surface shots

The initial homogeneous P-wave velocity model is derived from the records of 11 calibration shots (150 g explosives in 25 cm deep boreholes) at various locations in the upper part of the unstable slope within and around the seismic network. Wave velocities clearly differ for wave paths north and south of the back scarp. In addition, the recorded waveforms are very complex and partly strongly attenuated indicating scattering and the presence of small-scale heterogeneities. We use the shot recordings to both calibrate the velocity model and test the ability of our method to locate microseismic events.

An example of a shot record in Fig. 8 shows that both seismic and acoustic waves are recorded. To eliminate the short-period acoustic waves, we apply a low-pass filter with 40 Hz corner frequency. A range of P-wave velocities from 250 to 4000 m/s is tested and the success of the location procedure is assessed by maximising the stack enhancement and minimising the location error expressed by the distance to the true shot location. These criteria result in an optimum P-wave velocity of 1500 m/s, for which the mean location error amounts to 36 m. Figure 9 shows the true as well as determined shot locations including the location error estimate. In most cases, the location error ellipse comprises the true shot position.

3.4 Event magnitudes

Similar to standard seismic magnitude scales, we define the event size on a logarithmic scale. Due to the complex propagation paths in the fractured rock body, we do not apply a correction for distance; instead, we use the traces showing the highest maximum amplitude and take their logarithm; the 80th percentile of maximum amplitudes is used. This approach is justified by the short epicentral distance and shallow depth of the located events, which results in short hypocentral distances.
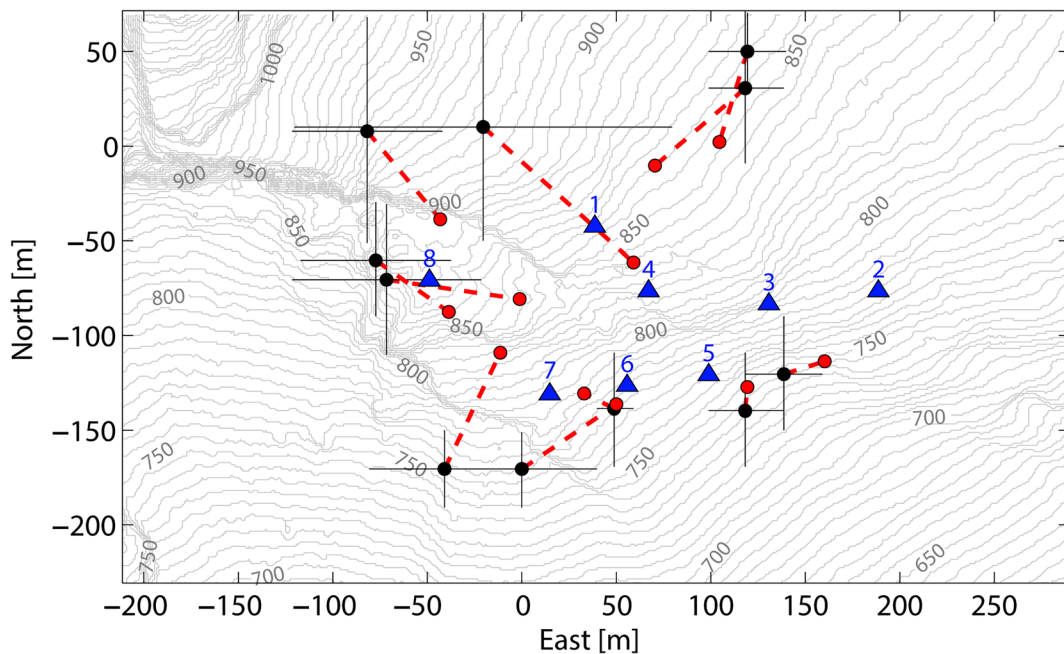

Fig. 9 Locating the 11 calibration shots employing the back-projection location method: geophones (blue triangles), true shot locations (red circles) and determined shot locations (black circles and crosses indicating the location error estimate) are shown. Note that in most cases, the true location error is in the range of the error estimate. Background: contour lines representing slope topography (height in metres)
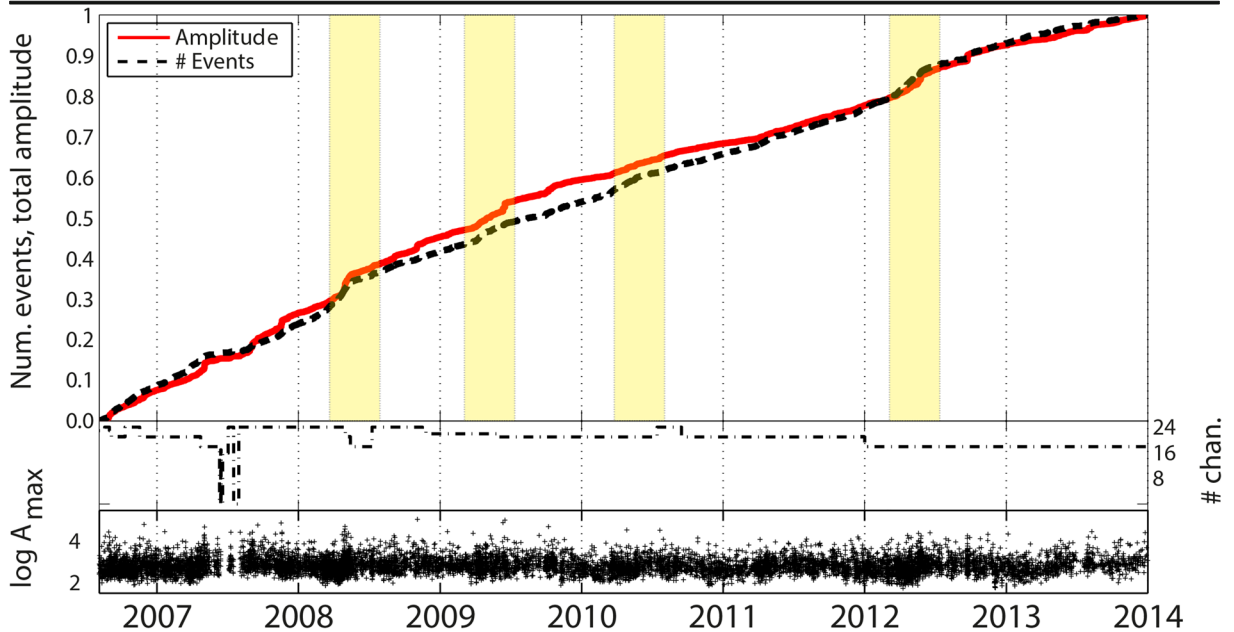
Fig. 10 Temporal activity of the Åknes rockslide represented by the cumulative number of events (dashed black line), the cumulative event amplitude (solid red line) and logarithmic event amplitudes (black crosses in lowermost panel). The middle panel illustrates the number of operating channels displayed by a dot-dashed line. Periods of increased activity are highlighted in yellow

4 Results and interpretation

We apply the event classification approach to seismic data recorded during the period 5 August 2006–31 December 2013. Of the total of 55,000 events processed, 30,000 are classified as microseismic events or rockfalls and are located by the back-projection stacking method. Based on
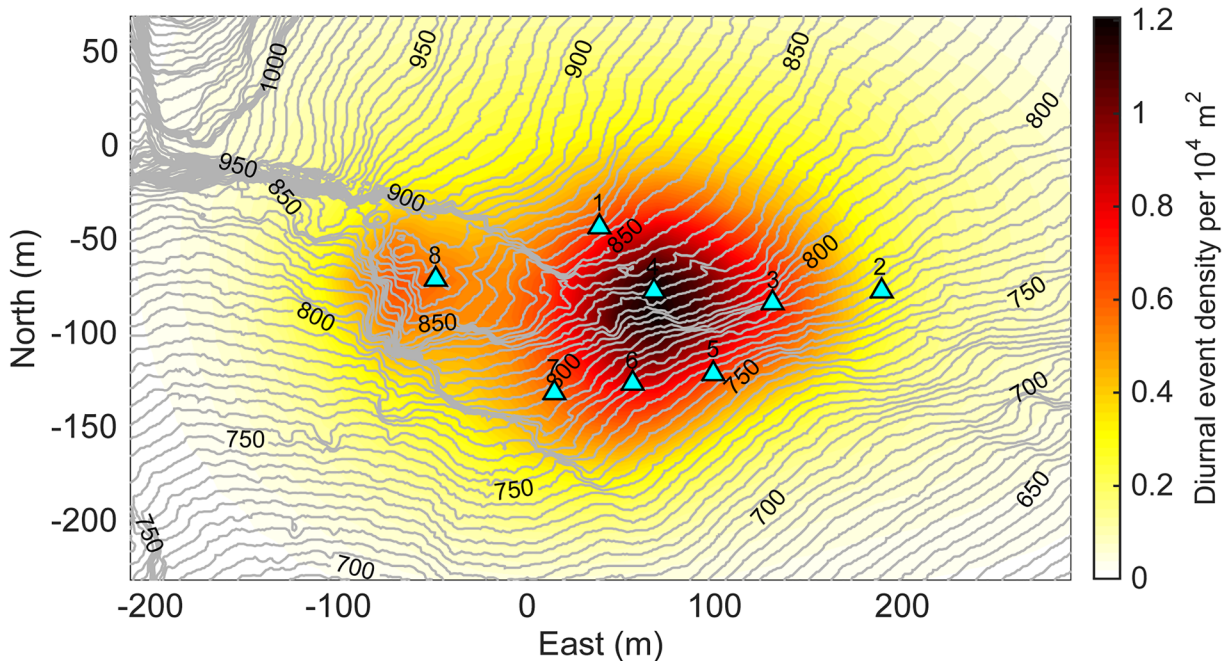

Fig. 11 Diurnal areal density (normalised to 10,000 m²) of epicentres of located events for the whole analysed period 2006–2013 on top of the digital elevation model indicated by isolines. In total, 10,580 microseismic and rockfall events with location errors lower than 50 m are used for computing the density

extensive tests and visual verification of seismograms and corresponding locations, we interpret the hypocentres of events with at least 8 recording channels used for location. We also require a minimum stack enhancement η of 1.05 and exclude events whose location lies at the edge of the grid.

4.1 Rockslide activity in 2006–2013

In total, 7100 microseismic events and 4343 rockfall events are successfully located employing the above quality criteria. The rockslide activity emerges as steady (Fig. 10) with few periods of increased activity occurring usually in late spring.
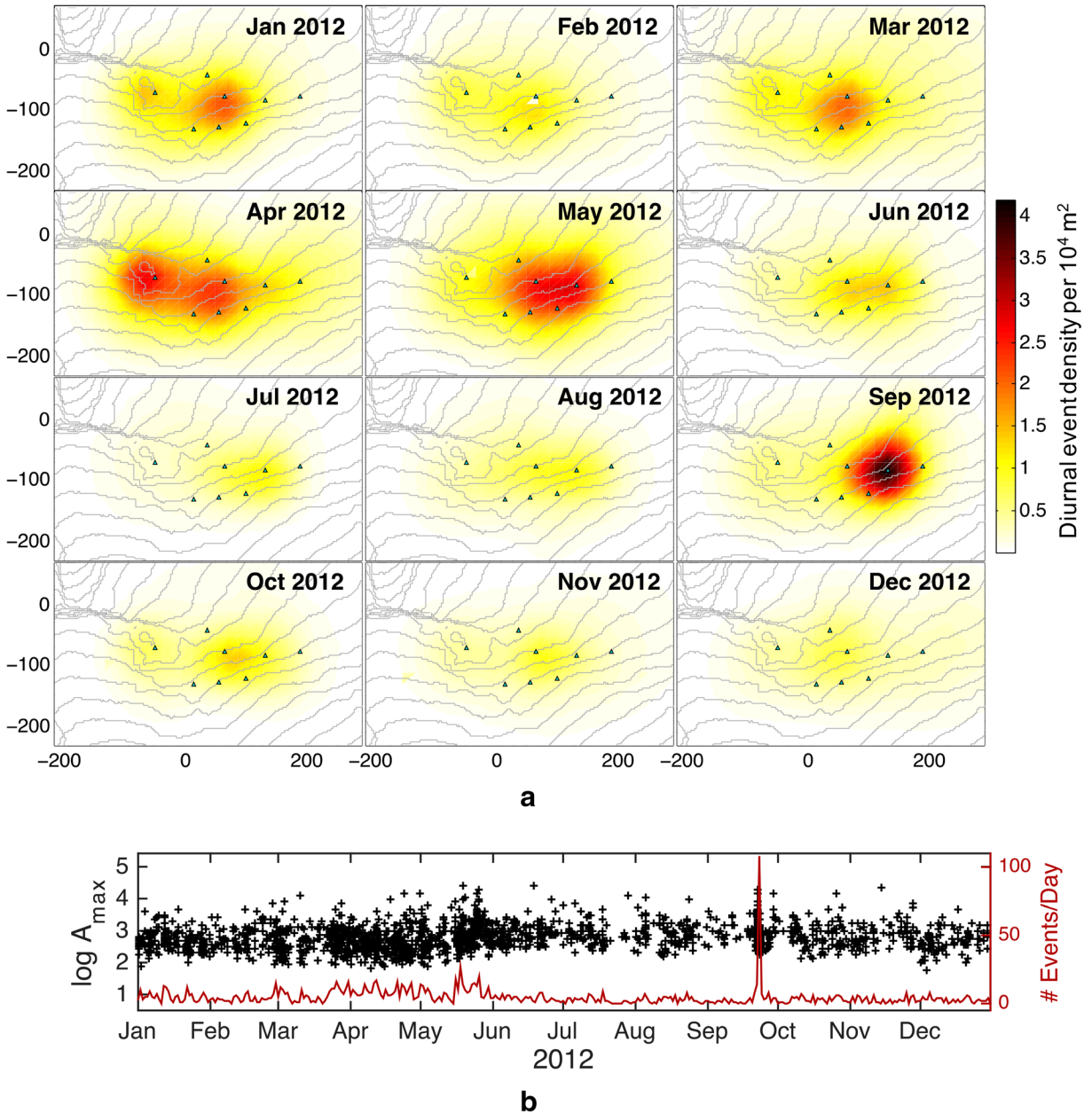

Fig. 12 Microseismic activity of the Åknes rockslide during 2012. **a** Diurnal event density per 10,000 m² area; black triangles show the local seismic network. **b** Temporal evolution of activity showing daily rate of events (red line) and event size represented by logarithmic maximum event amplitude (black crosses)

As described above, the location procedure deter-
mines horizontal (x_0, y_0) source coordinates only. For
the year 2011, we tested several potential event depths in
addition (− 40 m, − 20 m, 0 m, 20 m, 40 m and 60 m). Of
the 11,443 successfully located events, the vast majority
shows higher stack amplitudes for zero depth; only 675
events better fit a deeper hypocentre.

Since location errors are relatively large and compa-
rable with the interstation distance, we favour presenting
the spatial density of epicentres (Fig. 11) instead of
individual event locations. To this end, we count the
number of events on a rectangular horizontal grid with
20 m spacing and account for the location error by
expanding each epicentre into the adjacent cells using
weights derived from a normal distribution with stan-
dard deviation equal to the location error estimate. This
way, a sufficiently smooth density plot is achieved.
Instead of employing an event count, we also tested
visualising the cumulative amplitude of the events and
found that the resulting plot appears very similar.

In Fig. 11, the diurnal spatial density of source
positions of local events and rockfalls normalised
to 10,000 m² for the whole analysed period 2006–
2013 is shown. Two maxima of occurrence are
found: the first one in the centre of the area close
to geophone no. 4 and the second one at the
western edge close to geophone no. 8. The first
maximum is most probably related to the back
scarp that strikes between geophones no. 4 and
no. 3 and experiences almost continuous deforma-
tion. Below, we discuss a burst of seismic activity
that occurred close to geophone no. 3 in 2012.
The second maximum is related to the high cliff
above geophone no. 8 (see Fig. 2), which is the
source of frequent rockfalls.

4.2 The 2012 block collapse

The temporal evolution of seismic activity in Fig. 12
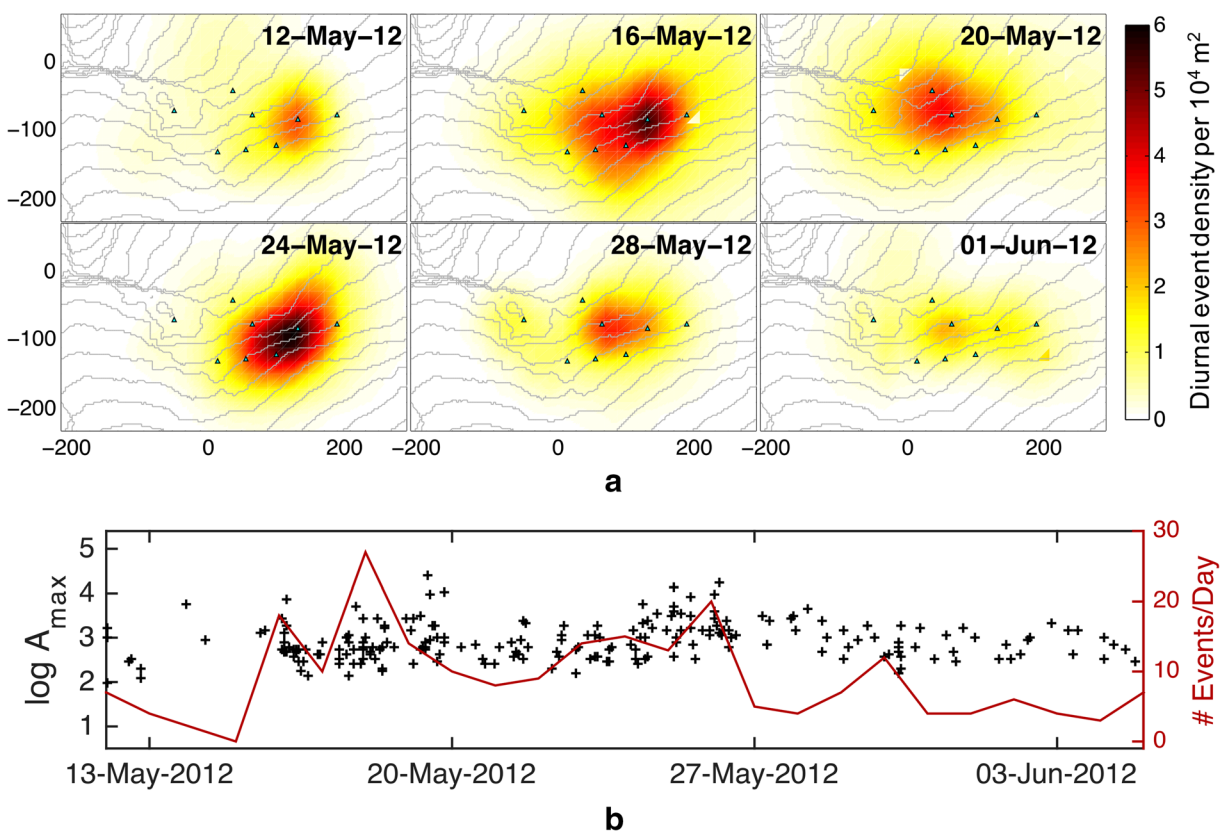shows elevated seismicity rates during two periods in

Fig. 13 Microseismic activity of the Åknes rockslide during the increased seismic activity in May 2012 displayed in 4-day intervals starting on May 12. **a** Diurnal event density per 10,000 m² area. **b** Temporal evolution of activity. For details, see caption of Fig. 12

2012. Thus, we investigated these bursts in activity in more detail in order to assess their origin. The monthly plots depicted in Fig. 12 show that the event density per 10,000 m² exceeds the value of two events per day during the months of January, March, April, May and September. It transpires that in May, besides the two active zones close to geophones no. 4 and no. 8 (see Fig. 11), a new area is activated close to geophone no. 3 and—after 3 months of quiescence—is reactivated in September in an intense burst. Both these bursts are also recognisable in the magnitude-time plot as clusters in mid-May and late September.

A closer look at the period of mid-May (Fig. 13) shows that there were two phases of activity: between May 16th and 20th as well as between May 24th and 27th: 211 events were located during this period. In contrast to this rather slow rockslide activity, the burst in late September demonstrates that much faster fracturing of the rock mass may occur (Fig. 14). On 22nd

September 2012, in total, 83 events have been successfully located close to geophone no. 3 in the course of only 3 h between 15 and 18 o'clock. Only negligible activity occurs during the few days before and after the burst.

It was reported by observers working on the slope that on 22nd September 2012, a block collapse occurred at about 4 o'clock in the afternoon close to geophone no. 3 and that it was preceded by a larger rockfall half an hour in advance (Fig. 15). The block that has as length of about 30 m detached from the back scarp and dropped about 1–2 m. Based on this verification, we derive that the burst of activity in May 2012, having the same location as that of September 2012, was related either to fracturing of the back scarp at the same place or to a preparation phase of this block collapse. This ground truth observation confirms that (i) the automatic location method is capable of locating microseismic events in the area of the seismic network with sufficient accuracy of tens of metres and (ii) the
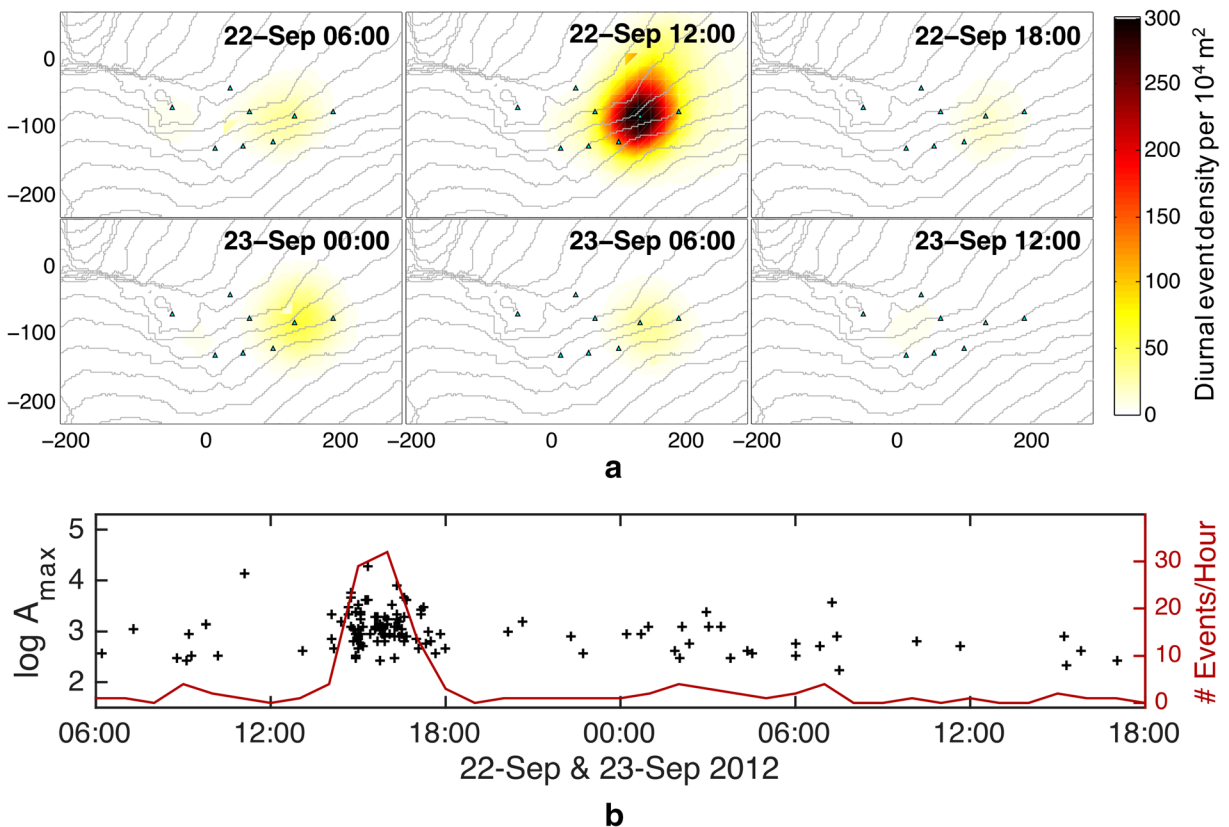

Fig. 14 Microseismic activity of the Åknes rockslide during the burst on 22nd September 2012 presented in 6-h intervals starting at the indicated time. **a** Diurnal event density per 10,000 m² area; note that its maximum is by two orders higher than in Figs. 12 and 13, because the peak of the 22nd September afternoon is scaled to 1 day of duration. **b** Temporal evolution of activity. For details, see caption of Fig. 12
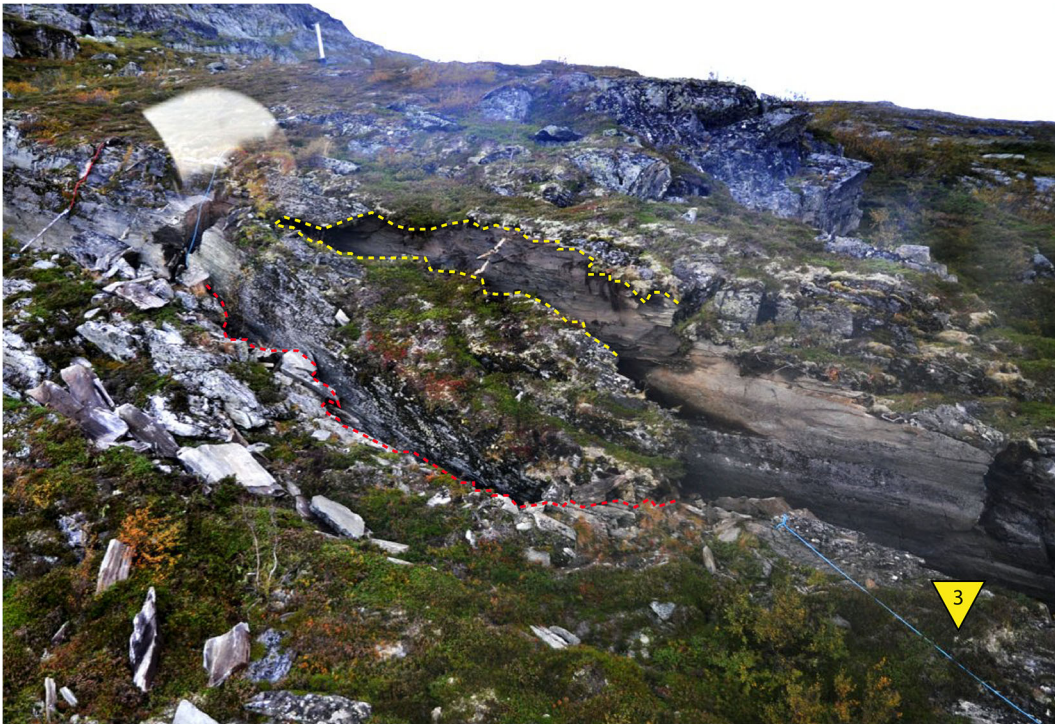
Fig. 15 Photograph of a block collapse at the back scarp obtained from a helicopter (courtesy L. H. Blikra). The length of the newly created fracture indicated by the yellow dashed line is about 30 m. The lower bound of the block is highlighted by the red dashed line. The approximate position of geophone no. 3 is shown by a yellow triangle

microseismic events recorded by the seismic network and located by the back-projection method originate within the body of the rock slope and are related to its disintegration or potentially to sliding on the detachment fault.

4.3 Comparison with meteorological data

In order to gain an overview on the temporal characteristics of event occurrence, we compared the monthly rate of events with meteorological data from the NVE meteorological station at 900 m a.s.l. (Figs. 16 and 17). Whereas we analysed event locations for the period January 2006 to December 2013, the available meteorological data cover the time period January 2009 to December 2014; therefore, we compare only yearly averages.

Grøneng et al. (2011) compared displacements measured by five extensometers and two laser sensors installed in the back scarp with meteorological data for the period November 2004 to August 2008. Their main findings are that water from snowmelt causes the largest annual deformation event (mid-March throughout May), whereas no significant

acceleration phases are recorded in summer and early autumn (mid-June throughout September). In addition, periods of heavy precipitation in combination with air temperature fluctuations around 0 °C seem to cause acceleration phases in autumn. The slope also seems to be stable in late winter (mid-January to mid-March) due to frozen conditions and the presence of a permanent snow cover. In addition, they note that the meteorological effects on the displacement in the back scarp are less prominent in the second half of the measurement period (September 2006 to August 2008) compared with the first half of the measurement period (September 2004 to August 2006).

In Fig. 16, the relations between monthly rate of events and precipitation (a) as well as temperature (b) is displayed (both averaged over the years of measurements). In agreement to Grøneng et al. (2011), we observe the largest number of events in April at the time of snowmelt (once the average temperature increases above 0 °C). However, unlike them, we do not see a correlation with precipitation, which might be caused by the fact that our period of observation only coincides

Fig. 16 **a** Comparison of monthly rate of events (red bars) averaged over 8 years of measurement (2006–2013) with precipitation in mm (black curve) averaged in 8-day bins over 6 years of measurement in 2009–2014. **b** Same as above, but monthly rate of events is compared with temperature in °C; black horizontal line marks 0 °C
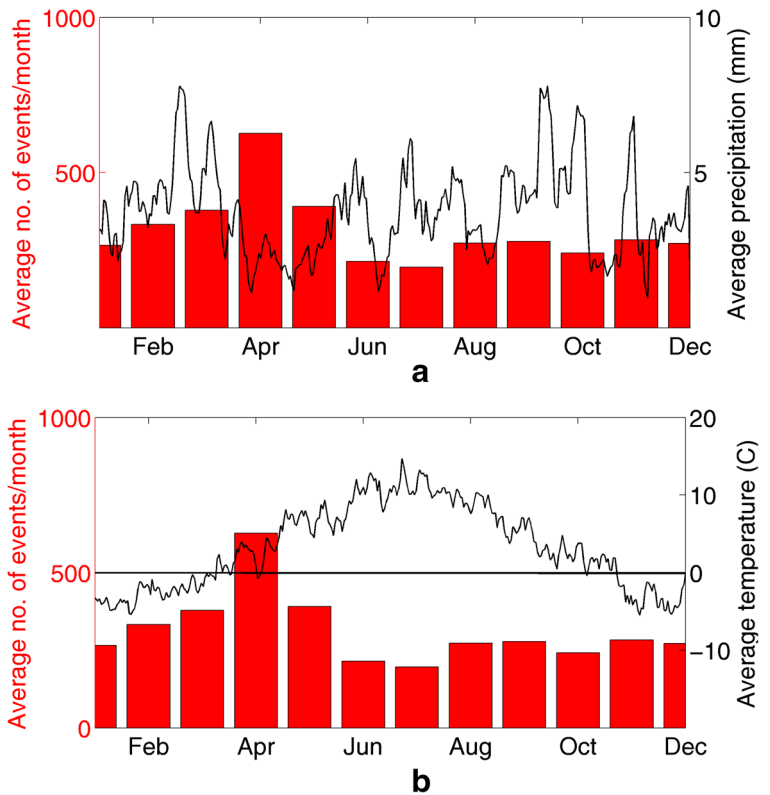
with theirs for about 2 years from January 2006 to August 2008 corresponding to the period where they find a less pronounced relation between meteorological data and displacement. Interestingly, the lowest number of events occurs during the warmest months of June and July fitting the observations of Grøneng et al. (2011) that no significant acceleration phases are recorded in summer.

Figure 17 a displays distribution curves of relative event magnitudes for three periods of the year: snowmelt (April), summer (May to October) and winter (November to March). Due to the different length of these time periods, the curve has been normalised by the maximum number of events. Figure 17 b compares the monthly number of events for two types of events: microseismic events and rockfalls. Both event types occur most often during the period of snowmelt in April. Whereas the number of both event types is similar throughout the summer and autumn, the number of microseismic events is higher during winter (November to March). Especially in January, the number of rockfalls is extremely low, probably due to a similar reason. Grøneng

et al. (2011) give for the absence of deformation within that period: stable frozen conditions and the presence of a snow cover.

Although the number of events during snowmelt is large, the event size is lower than for events occurring in summer (Fig. 17a). Since only triggered data is stored, we cannot exclude that in summer, only larger magnitude events are detected due to a higher noise floor. Nevertheless, since Grøneng et al. (2011) observe that the snow melting period causes the largest annual deformation event, this could mean that this deformation event is composed of a large number of small deformations episodes.

In general, coupling the event rates to the observations by Grøneng et al. (2011), it emerges that deformation observed at the back scarp is accompanied by microseismic events. Considering that most events shows higher stack amplitudes for zero depth, we consider that it is more likely that events occur on fractures within the slope body, e.g. the second set of fractures observed by Ganerød et al. (2008) running sub-parallel to the slope, instead of on the basal sliding plane. Thus, their high number of

Fig. 17 **a** Distribution curves of relative event sizes for three periods of the year: snowmelt (blue line), summer (green line) and winter (red line). **b** Comparison of monthly number of events for two event types: microseismic events (blue bars) and rockfalls (red bars)
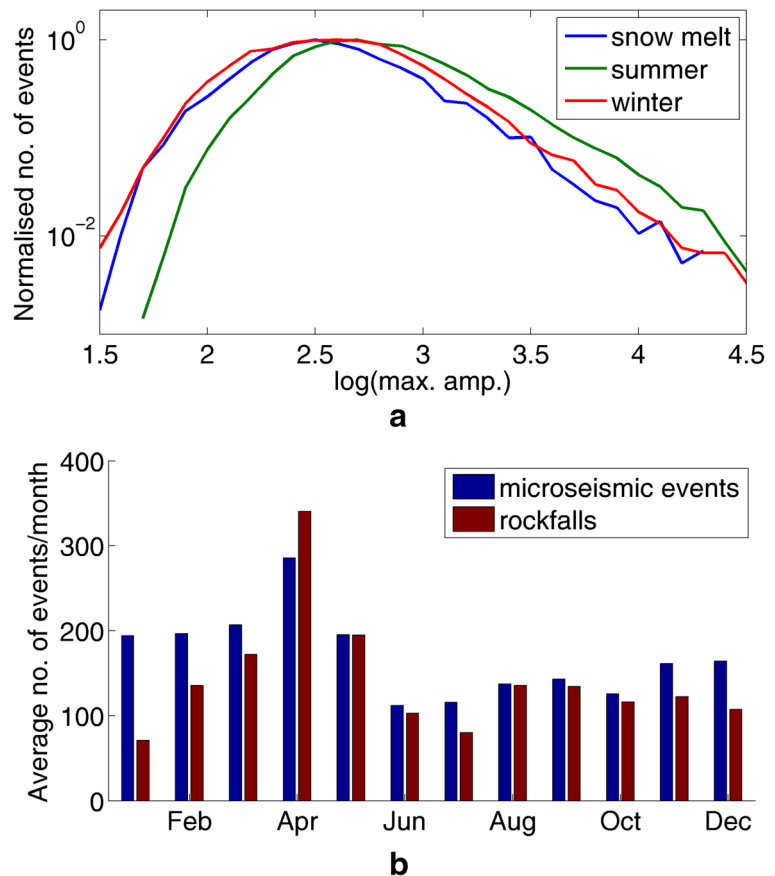
occurrence simultaneously with the largest annual deformation implies that this shallow fracture network is activated by movement on the deeper sliding plane supporting the hypothesis by Ganerød et al. (2008) based on the analysis of the fracture network. In turn, the fact that the frequency of occurrence of the fractures representing older reactivated structures decreases with depth (Ganerød et al. 2008) reinforces our findings of the microseismic events originating close to the surface.

5 Discussion

We applied an automatic event classification and back-projection location method to the triggered seismic data recorded by a seismic network on the rockslide in Åknes, Norway. Based on signal characteristics, the events were classified into five event types: microseismic events, rockfalls, distant events, noise and electronic spikes. Of the roughly 50,000 events recorded during

the investigated period 2006–2013, 30,000 events were classified as local microseismic events and rockfalls, i.e. occurring in the investigated area of the rockslide.

The back-projection approach for event location outperformed previous attempts for application of standard location methods based on arrival time measurements. One possible reason is the small aperture of the seismic network of 200 m, which implies travel times of about 0.1 s. Achieving a location error smaller than the network aperture requires arrival time measurements with the precision of only a few milliseconds, which is not feasible due to the complicated seismograms exhibiting frequently emergent onsets and poorly defined polarisation caused by irregular wave propagation in the strongly fractured rock slope. The complex polarisation also renders it almost impossible to identify S-waves in the seismograms if these are present at all in the wavefield. On top of that, the complex topography and strongly fractured medium do not allow for building a sufficiently accurate velocity model.

In contrast to arrival time picking, the migration-based location methods use a characteristic function, whose amplitude is proportional to the probability of wave arrival. By shifting the characteristic functions of individual stations to the hypocentre and subsequently stacking the traces, the uncertainty of the arrival time is implicitly accounted for. In order to make the location procedure more effective and because of not well-defined arrivals, we limit the unknown coordinates to the surface of the digital elevation model, which is justified by the near-surface character of the monitored seismicity. We use the STA/LTA ratio as characteristic function and verify the location capability of the method on 11 calibration shots, whose epicentres are determined with a location error lower than 36 m.

Application of the procedure to the Åknes data from 2006 to 2013 resulted in successful location of 11,443 microseismic events and rockfalls. However, no significant difference between the source positions of microseismic events and rockfalls is found. This can probably be attributed to the fact that both types of events occur along the whole rock slope.

The resulting locations show a number of periods of increased activity. We analysed in detail two bursts in activity from May and September 2012 and find that these correspond to activating a relatively quiet area close to geophone no. 3. By comparing with visual observations, it is recognised that these bursts of activity are related to the collapse of a 30 m long block of rock. This verification has proven the capability of the back-projection location method for monitoring the activity and its automatic event location that could be applied in real time within the early warning system; the processing of one event takes less than 1 s on a standard laptop computer.

Comparison of seismic activity of the slope with meteorological data provides several interesting findings. While no clear relation to precipitation was found, air temperature appears to influence sliding: the rate of events doubles in spring when temperatures exceed 0 °C, which probably results in acceleration of the rockslide due to snowmelt. In terms of seismic event characteristics, three seasons can be found: (i) winter (November-March), mostly microseismic events with smaller amplitudes; (ii) snowmelt period (April), mostly rockfalls with smaller amplitudes; (iii) summer (May-October), both microseismic events and rockfalls with larger events amplitudes.

6 Conclusions

The back-projection approach for event location outperforms previous attempts of applying a standard location method based on arrival time measurements to locate approximately 11,500 out of 30,000 events classified as local microseismic events and rockfalls occurring between 2006 and 2013. The approach is verified by locating surface shots and by application to a collapse of a block on the slope. No significant difference between the geographical origin of microseismic events and rockfalls has been found. The largest number of events is observed at the time of snowmelt. The number of observed events averaged over periods of the year agrees with the acceleration and deceleration phases of deformation observed by Grøneng et al. (2011). Most likely, the events occur on the shallow fracture network, which seemingly is activated by movement on the deeper basal sliding plane.

References

ÅTB (2010) Åknes: state of instrumentation and data analysis. Report 02.2010

Blikra LH, Longva O, Harbitz CB, Løvholt F (2005) Quantification of rock-avalanche and tsunami hazard in Storfjorden, Western Norway. In Senneset K, Flaate K, Larsen JO (eds.): Landslides and avalanches. Proc 11th Int Conf Field Trip on Landslides, Norway, 1–10 September 2005. Taylor & Francis Group, London: 57–63

Blikra LH, Longva O, Braathen A, Anda E, Dehls J, Stalsberg K (2006) Rock-slope failures in Norwegian fjord areas: examples, spatial distribution and temporal pattern. In Evans SG, Scarawcia Mugnozza G, Strom AL, Hermanns RL (eds.):

Landslides from massive rock slope failure. NATO Science Series 49:475–496

Blikra LH, Kristensen L, Lovisolo M (2013) Subsurface monitoring of large rockslides in Norway: a key requirement for early warning. Ital J Eng Geol Environ 6:307–314

Braathen A, Blikra LH, Berg SS, Karlsen F (2004) Rock-slope failures in Norway; type, geometry, deformation mechanisms and stability. Nor J Geol 84:67–88

Frei C (2008) Groundwater flow at the Åknes rockslide site (Norway) - results of a multi-tracer test. Dissertation, ETH Zurich, Switzerland

Ganerød GV, Grøneng G, Rønning JS, Dalsegg E, Elvebakk H, Tønnesen JF, Kveldsvik V, Eiken T, Blikra LH, Braathen A (2008) Geological model of the Åknes rockslide, western Norway. Eng Geol 102:1–18

Gharti HN, Oye V, Roth M, Kühn D (2010) Automated micro-earthquake location using envelope stacking and robust global optimization. Geophysics 75(4):MA27–MA46

Gomberg J, Schulz W, Bodin P, Kean J (2011) Seismic and geodetic signatures of fault slip at the Slumgullion landslide natural laboratory. J Geophys Res 116:B09404-1–B09404-20

Grigoli F, Cesca S, Amoroso O, Emolo A, Zollo A, Dahm T (2014) Automated seismic event location by waveform coherence analysis. Geophys J Int 196:1742–1753

Grøneng G, Christiansen HH, Nilsen B, Blikra LH (2011) Meteorological effects on seasonal displacements of the Åknes rockslide, Western Norway. Landslides 8:1–15

Harbitz CB, Glimsdal S, Løvholt F, Kveldsvik V, Pedersen GK, Jensen A (2014) Rockslide tsunamis in complex fjords: from an unstable rock slope at Åkerneset to tsunami risk in western Norway. Coast Eng 88:101–122

Heincke B, Günther T, Dalsegg E, Rønning JS, Ganerød GV, Elvebakk H (2010) Combined three-dimensional electronic and seismic tomography study on the Åknes rockslide in Western Norway. J Appl Geophys 70(4):292–306

Helmstetter A, Garambois S (2010) Seismic monitoring of Séchilienne rockslide (French Alps): analysis of seismic signals and their correlation with rainfalls. J Geophys Res 115: F03016-1–F03016-15

Kao H, Shan SJ (2007) Rapid identification of earthquake rupture plane using source-scanning algorithm. Geophys J Int 168: 1011–1020

Kinscher J, Bernard P, Contrucci I, Mangeney A, Piguet JP, Bigarre P (2014) Location of microseismic swarms induced by salt solution mining. Geophys J Int 200:337–362

Kveldsvik V (2008) Static and dynamic stability analyses of the 800 m high Åknes rock slope, Western Norway. Dissertation, NTNU Trondheim, Norway

Kveldsvik V, Nilsen B, Einstein HH, Nadim F (2008) Alternative approaches for analyses of a 100,000 m³ rock slide based on Barton-Bandis shear strength criterion. Landslides 5:101–112

Lacroix P, Helmstetter A (2011) Location of seismic signals associated with microearthquakes and rockfalls on the Séchilienne landslide, French Alps. Bull Seismol Soc Am 101:341–353

Nordvik T, Grøneng G, Ganerød G, Nilsen B, Harding C, Blikra L (2009) Geovisualization, geometric modeling and volume estimation of the Åknes rockslide, Western Norway. Bull Eng Geol Environ 68(2):245–256

Oppikofer T, Jaboyedoff M, Blikra L, Derron M-H, Metzger R (2009) Characterization and monitoring of the Åknes rockslide using terrestrial laser scanning. Nat Hazards Earth Syst Sci 9:1003–1019

Salvoni M, Dight PM (2016) Rock damage assessment in a large unstable slope from microseismic monitoring - MMG Century mine (Queensland, Australia) case study. Eng Geol 210:45–56

Spillmann T, Maurer H, Green AG, Heincke B, Willenberg H, Husen S (2007) Microseismic investigation of an unstable mountain slope in the Swiss Alps. J Geophys Res 112: B07301-1–B07301-25

Vlček J, Fischer T, Vilhelm J (2016) Back-projection stacking of P- and S-waves to determine location and focal mechanism of microseismic events recorded by a surface array. Geophys Prospect 64(6):1428–1440

Withers M, Aster R, Young C (1999) An automated local and regional seismic event detection and location system using waveform correlation. Bull Seismol Soc Am 89(3):657–669